LANGMUIR

pubs.acs.org/Langmuir Article

Predicting the Dynamics and Steady-State Shape of Cylindrical Newtonian Filaments on Solid Substrates

Amir Azimi Yancheshme, Giuseppe R. Palmese, and Nicolas J. Alvarez*

Cite This: *Langmuir* 2023, 39, 10495−10503 Read Online

ACCESS | Metrics & More | Article Recommendations | Supporting Information

ABSTRACT: The spreading of liquid filaments on solid surfaces is of paramount importance to a wide range of applications including ink-jet printing, coating, and direct ink writing (DIW). However, there is a considerable lack of experimental, numerical, and theoretical studies on the spreading of filaments on solid substrates. In this work, we studied the dynamics of spreading of Newtonian filaments via experiment, numerical simulations, and theoretical analysis. More specifically, we used a novel experimental setup to validate a 2D moving mesh computational fluid dynamics (CFD) model. The CFD model is used to determine the effect of processing and fluid parameters on the dynamics of filament spreading. We experimentally showed that for a Newtonian filament, the same spreading dynamics and final shape are obtained when the initial radius is constant, independent of the magnitude in printing parameters. In other words, the only important parameter on the spreading of filaments is the initial filament radius. Using a numerical model, we showed that the initial filament radius manifests itself in two important dimensionless parameters, Bond number, Bo, and viscous timescale, τ_μ. Furthermore, the results clearly show that the dynamics of spreading are governed by the static advancing contact angle, θ_s. These three parameters determine a master spreading curve that can be used to predict the spreading of cylindrical filaments on flat substrates. Finally, we developed a theoretical model that was parameterized using experimental data to correlate the steady-state shape of filaments with Bo and θ_s. These results are particularly applicable for predicting and controlling the dynamics of filaments in DIW and other extrusion-based processes.

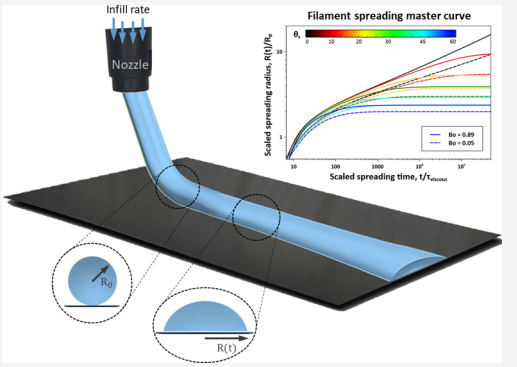

INTRODUCTION

Numerous fields such as coating, microfluidics, ink-jet printing technologies, and additive manufacturing have shown significant interest in the spreading of spherical droplets on solid substrates.[1−4] Thus, droplet spreading dynamics have been extensively studied for over four decades, including a recent general theory that employs computational fluid dynamics (CFD) and careful experimentation to quantify the dynamics of droplet spreading on solid substrates.[5] This recent theory predicts the spreading of droplets for a given Bond number, Bo (relative effect of gravity), and static advancing contact angle, θ_s. However, not all droplet applications are spherical in shape, such as those involving 3D printing techniques like fused deposition modeling (FDM) and direct ink writing (DIW), which deposit cylindrical droplets/beads, a.k.a filaments, onto solid substrates and previously printed layers to form a complex 3D shape.

The spreading of cylindrical beads from line to line and layer to layer plays a crucial role in determining the final 3D part shape, quality, and fidelity.[6,7] Unfortunately, there are only a few studies that examine the experimental or theoretical aspects of filament spreading. One reason for this is the infinite interfacial instability of deposited filaments, which causes them to break up into spherical beads over time.[8] Despite this limitation, cylindrical filaments have become a useful method of 3D printing, whereby the instability is prevented via stabilizing elastic stresses induced by reacting a thermoset resin to form a gel network,[1,3,9] or through rheological modifiers that thicken after deposition.[6,10−12] In this study, we present a general theory for the spreading of cylindrical filaments on solid substrates that considers Newtonian fluids with varying effects of gravity and static advancing contact angles. Although this theory does not currently account for the evolution of elastic stresses, it provides a baseline or upper bound for the spreading that would be observed experimentally in 3D printing methods.

When an extruded filament comes into contact with a surface, the curvature gradients (i.e., Laplace pressure) and/or gravitational forces initiate a spreading process denoted by lateral movement of the contact line from the contact point, known as basal radius. The rate of the spreading process is determined by fluid inertia and viscous dissipation,[13] until the

Received: April 11, 2023
Revised: June 5, 2023
Published: July 20, 2023

capillary force, gravitational force, and static advancing contact angle, θ_s, balance the Young−Laplace equation[14] and equilibrium is established. While the cylindrical geometry of deposited filaments is anticipated to have a quantitative impact on spreading, there are numerous qualitative effects that are expected to resemble the spreading of spherical droplets.[5,15] More specifically, we would expect similar scaling arguments of the spreading dynamics and shape of the filament with Bond number, fast and slow spreading dynamics dominated by inertia and viscosity, respectively, and finally a power-law scaling of the slow spreading regime with time. For example, the Bond number, Bo, defined as the ratio of gravitational and capillary forces, should determine the relative importance of gravity on the shape and spreading dynamics, and it distinguishes two important spreading regimes: the capillary and gravitational regimes. In the capillary regime, Bo $\ll$ 1, the effect of gravity can be ignored and the cross-sectional interface is a circular segment.[16] While in the gravitational spreading regime, Bo $\gg$ 1, gravity dictates the spreading behavior and the cross-sectional shape is flattened.[16]

While the spreading of spherical droplets has been extensively investigated via experiments,[13,17,18] theory,[19−26] and computational methods,[5,27] the spreading of filaments has received little attention. One exception is the work by Starov et al.,[15] which developed a theoretical model for the spreading of a 2D symmetric cylindrical filament in the capillary and gravitational spreading limits. The model used an empirical geometrical factor for the capillary spreading regime to reduce the complexity of the problem, which significantly limits its applicability. Moreover, the model is only limited to either ignoring the effect of gravity or considering gravity as the only driving force. In most of the practical cases, both capillary and gravity contribute to the spreading process which includes 0 < Bo < 1. However, one important result was the determination of a 1/7 and 1/5 power-law scaling of the spreading radius with time for the capillary and gravitational spreading regimes, respectively.[15] Note that this power-law behavior is significantly faster than that observed for spherical droplets.[5,13,28] Although this model is limited in predicting quantitative spreading dynamics, these results are useful in validating future theory and models.

As described above, the Bond number is a very important dimensionless parameter in understanding spreading dynamics. In other words, quantitative predictions of spreading dynamics and filaments shape require an *a priori* measure of the filament Bond number. However, the Bond number depends on the initial filament radius, which is a strong function of the deposition method. For example in DIW, parameters such as nozzle velocity, nozzle standoff height, infill flow rate, nozzle diameter, etc. significantly impact the final shape of the printed filament.[6,7,29] More specifically, it has been shown that increasing the nozzle velocity while keeping the infill flow rate constant decreases the amount of extruded material and results in filaments with a smaller basal radius.[6,7,30] Similarly, at fixed nozzle velocity and increasing infill flow rate, the basal radius increases.[6,7,30] Furthermore, the nozzle height can significantly influence the final bead shape by squeezing the fluid during deposition.[6,29] There are only a few studies on the effect of DIW operational parameters on the shape of the deposited filaments[7] and almost all of them are limited to highly loaded pastes with minimized spreading.[6,7,29−32] There is an important need for a quantitative relationship between printing parameters and the initial radius of the deposited filament and consequently its spreading dynamics, especially for the systems including medium to low-viscous fluids which undergo a considerable amount of spreading upon contact with the printing bed.

In this work, we use a novel experimental setup and computational modeling to develop a general theory of cylindrical filament spreading considering the specifics of the filament deposition process. More specifically, we introduce a comprehensive generalized theory for predicting the spreading of Newtonian filaments considering the effect of process parameters, gravity, and wettability. The spreading master curves that result from this work allow for the prediction of spreading dynamics of deposited filaments for use in additive manufacturing and other cylindrical filament deposition applications. The organization of the paper is as follows. We first study the effect of printing parameters, i.e., nozzle velocity, nozzle height, and infill flow rate on the spreading of Newtonian filaments in DIW aiming at finding the most influential parameter on the spreading. Then, we develop and validate a numerical 2D moving mesh model to simulate filament spreading dynamics. The results are organized into spreading master curves as a function of θ_s and Bo, which can be used to estimate the dynamic shape of a filament during the spreading. Furthermore, regarding the static shape, we developed an empirical model to predict the equilibrium shape of the deposited filaments as a function of Bo and θ_s.

MATERIALS AND METHODS

Experimental Setup. The deposition and subsequent spreading of filaments onto silica substrates (AmScope) were achieved using a modified Delta Wasp 2040 Clay Printer (WASP), see Figure 1, a mid-

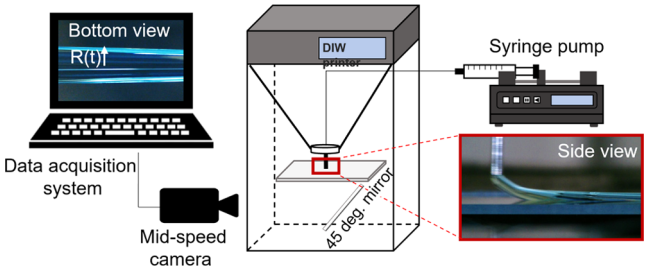

Figure 1. Experimental setup used for filament deposition and monitoring spreading at different operating conditions.

speed camera (HAYEAR, HY-2307, 2 M pixels with pixel size of 1.43 × 1.43 μm and 60 fps) with a microscope zoom lens, and an 18 gauge needle (ID = 0.834 mm) fed by a syringe pump (HARVARD Apparatus, PHD 2000) to deposit the filaments. A custom-built platform with a 45° flat mirror underneath the microscope glass slides (AmScope) was used to monitor the spreading of the deposited filament from the bottom view. Prior to each experiment, the silica substrate was washed with isopropanol (VWR, CAS No. 67-63-0) and subsequently rinsed using DI water (18.2 MΩ cm EMD Millipore Corporation). As a best practice for reproducible results, a new microscope glass slide was washed prior to each experiment. Each spreading experiment was performed at least three times, and the data represent the average of all experimental data sets. Each spreading experiment was performed by depositing an ≈75 mm long single filament on the glass slide at a given nozzle velocity V_N, infill flow rate Q, and nozzle height H (see Figure 2). The spreading was analyzed near the middle of the filament so as to avoid beginning and end effects due to acceleration/deceleration of the printer head. The basal radius was measured ex situ using image analysis software, ImageJ (ImageJ.Ink, V. 1.46), and a custom Matlab script. A 3D printing resin

https://doi.org/10.1021/acs.langmuir.3c00973
Langmuir 2023, 39, 10495−10503

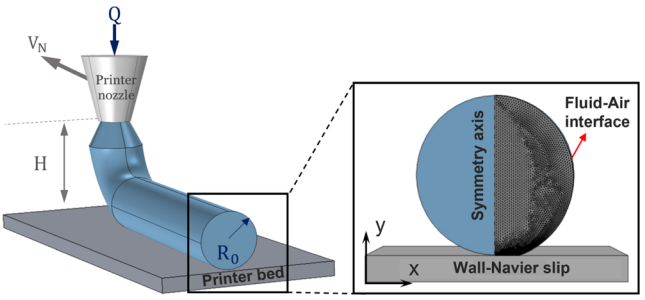

Figure 2. Schematic representation of cylindrical filament extruded from a nozzle (left) and a 2-dimensional view used in our simulations (right) showing the free triangular computational mesh used in simulations. Note the use of a finer mesh at the fluid−air interface to better resolve the movement of the free surface.

comprising bisphenol A glycerolate dimethacrylate (Bis-GMA 37.5 wt %), ethoxylated bisphenol A dimethacrylate (Bis-EMA 37.5 wt %), and 1,6-hexanediol dimethacrylate (HDDMA 25 wt %) called DA-2 was used[33] for all experiments. The physical properties of DA-2 including viscosity, surface tension, and density are 490 ± 50 Pa·s, 35.1 mN/m, and 1105 ± 1 kg/m^3, respectively, with a static advancing contact angle θ_s of 19.6 ± 1.4 on silica substrate.[33]

Numerical Modeling. The computational approach is very similar to that previously reported for spherical droplets.[5] We applied a two-phase moving mesh method to describe the free surface movement. The equations were solved using a finite element method (FEM) in COMSOL multiphysics v.5.6. considering a 2D symmetric framework. Figure 2 schematically shows the cylindrical 2D cross section of the filament, along with a typical mesh structure. Figure S1 shows the independence of the results to mesh grid spacing, see the Supporting Information. A mesh size criteria of $R_0/40$ was used for all simulations since finer mesh does not improve the reported accuracy. Note that the mesh was refined near the triple contact line by scaling the mesh points down by a factor of 0.2. Furthermore, an automatic remeshing constraint was applied to rebuild the entire domain when the quality of mesh falls below 0.1. We avoided full 3D simulation owing to both its high computational load and the onset of longitudinal capillary instability. In other words, this work considered the spreading of an infinitely long cylinder with no longitudinal interfacial instability.

Governing Equations. The unsteady Navier−Stokes (eq 1) and continuity (eq 2) were solved to determine the pressure p and velocity field ($\bar{u}$) over time. ρ and μ are the fluid density and dynamic viscosity, respectively.

$$\rho\left(\frac{\partial \bar{u}}{\partial t} + \bar{u}\cdot\bar{\nabla}\,\bar{u}\right) = -\bar{\nabla}\,p + \mu\nabla^2\bar{u} + \rho\bar{g} \quad (1)$$

$$\nabla\cdot\bar{u} = 0 \quad (2)$$

Equations 1 and 2 were solved subject to the following boundary conditions.

Boundary Conditions. The normal and tangential stress balance at the interface (eq 3) was applied to track the motion of the free surface, i.e., fluid−air boundary, S, as a function of time. At the solid−liquid interface, a Navier-slip condition (eq 4) with no penetration (eq 5) was utilized, where β is the slip length and is considered as 1/5× mesh size. Note that the spreading behavior is quite insensitive to the values of β.[5] Furthermore, at the triple contact line (i.e., intercept of the interface, substrate, and surrounding air), the tangential stress balance requires an additional condition. We have previously shown that the most appropriate condition is an equation relating the dynamic contact angle to the dimensionless contact line velocity, i.e., Ca. eq 6 was shown to work extremely well at capturing the spreading of spherical droplets and is employed unchanged in this work.[5,9]

$$\bar{n}\cdot(\bar{\bar{T}}^{I} - \bar{\bar{T}}^{II}) = \sigma(\bar{\nabla}\cdot\bar{n})\bar{n} - \bar{\nabla}\,\sigma \quad (3)$$

$$\bar{\tau}_f = \mu\frac{\bar{u}}{\beta} \quad (4)$$

$$\bar{u}\cdot\bar{n}_{wall} = 0 \quad (5)$$

$$\frac{\cos(\theta_s) - \cos(\theta_D)}{\cos(\theta_s) + 1} = \tanh(A\mathrm{Ca}^B) \quad (6)$$

where σ is the surface tension, $\bar{\bar{T}}$ is the total stress, i.e., $p\bar{\bar{I}} - \bar{\bar{\tau}}$, and the RHS of eq 3 represents the force per unit area due to σ. θ_D is the dynamic contact angle. Ca = $\mu\,\bar{u}/\sigma$ is the capillary number. A and B are fitting parameters equal to 7.32 and 0.702, respectively. More details are given in ref 5.

RESULTS AND DISCUSSION

Effect of Operating Parameters on Filament Spreading. There are four processing parameters that affect the shape of the filaments during deposition: infill flow rate, Q, nozzle diameter D_N, nozzle velocity, V_N, and nozzle height, H.[6,7] Note that all experiments were performed at a fixed needle diameter,

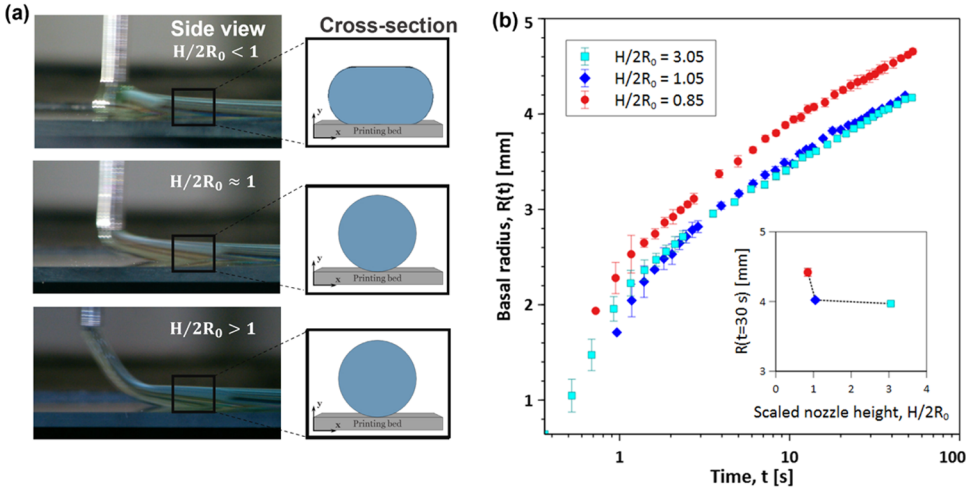

Figure 3. (a) Side-view image and cross-sectional schematic of filaments deposited at three different nozzle heights. (b) Experimentally measured basal radius versus time using D_N = 0.834 mm, Q = 6.67 mL/min, and V_N = 32.25 mm/s, at three different H values. The inset shows the magnitude of filament basal radius as a function of scaled nozzle height defined as $H/2R_0$.

https://doi.org/10.1021/acs.langmuir.3c00973
Langmuir 2023, 39, 10495−10503

D_N = 0.834 mm. The magnitude of each parameter was chosen to ensure uniform morphology of the deposited filament. Note that for a given D_N, there is a minimum Q below which the extruded fluid transitions from the jetting regime to the dripping regime.[34]

We now examine the effect of each parameter independently.

Effect of Nozzle Height. The effect of nozzle height on the shape of the filament cross section is an important relationship in DIW. As one might expect, when the filament height is large enough, there is no distortion of the filament by the nozzle. However, when the nozzle height is below a certain height, the filament will be compressed by the nozzle, leading to a noticeable distortion of the shape from spherical.[6,7,29] We are interested in developing a theoretical relationship between printing parameters and the critical height, h_c, where the filament shape is unaffected by the nozzle position. We expect that h_c is a function of the initial filament radius, R_0, which is a function of printing parameters.

Wang and Shaw[29] proposed a relationship between printing parameters and h_c considering a rectangular cross section and conservation of mass, i.e., $h_c = Q/V_nD_n$. However, the initial cross section of the extruded filament is more circular than rectangular, which means that Wang's model significantly underpredicts h_c regardless of fluid viscosity. An example of the poor predictability of Wang's model is found in Jang et al.[7] However, an improvement of Wang's model can be achieved by considering a circular cross section.

According to mass conservation, the nozzle infill flow rate is given by, i.e., $Q = V_NA_f$. A_f is the filament cross-sectional area far from the nozzle, which before spreading is assumed to be a circular cross-sectional area of radius R_0, i.e., $A_f = \pi R_0^2$. Substituting A_f into mass conservation gives

$$R_0 = 0.5\left(\frac{Q}{\pi V_N}\right)^{0.5} \tag{7}$$

Equation 7 gives R_0 as a function of the nozzle velocity and infill flow rate. This differs from Wang's model via a power-law of 0.5 and no explicit dependence on D_n, and agrees with that reported in refs 35, 36. This equation will be used in later studies to determine the value of R_0 for scaling purposes.

Figure 3 shows the basal radius as a function of time for DA-2. The experiments were performed using D_N = 0.834 mm, Q = 6.67 mL/min, V_N = 32.25 mm/s, and three different values of H. Depending on the value of H with respect to R_0 (using eq 7), two different regimes were observed: (i) $H/2R_0 < 1$, and (ii) $H/2R_0 \geq 1$. When $H/2R_0$ is greater than unity, the spreading is not affected by the nozzle height (dark and light blue data sets in Figure 3b). In the absence of any distortion of the filament cross section by say a squeezing flow, the surface tension acts to maintain a circular cross section (i.e., minimum surface energy). Thus, the initial shape of the filament right before deposition can be assumed to have a circular cross section (see Figure 3a). While for $H/2R_0$ less than unity, the nozzle compresses the filament and the initial cross-sectional shape is oblong (see Figure 3a). Given that all printing parameters are identical, except H, we would have expected the spreading to be the same. However, Figure 3b clearly shows that compression caused by the nozzle significantly affects the spreading dynamics of the filament (red data sets in Figure 3b). To further confirm our observations, we showed the effect of nozzle height on the spreading at two different operating conditions, see Figure S2. The inset of Figure 3b shows the filament basal radius at t = 30 s as a function of scaled nozzle height ($H/2R_0$). For $H < h_c$, the final basal radius is larger than for the case of $H > h_c$. This observation is in line with that reported by Jin et al.[6]

Effect of Nozzle Velocity and Infill Flow Rate. Figure 4 shows three experiments for different printing parameters.

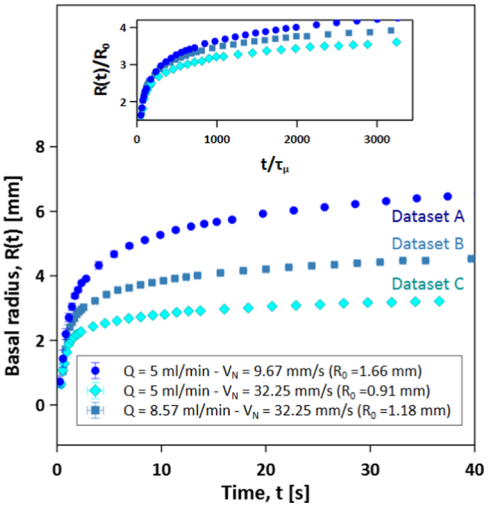

Figure 4. Effect of nozzle velocity and infill flow rate on basal radius as a function of time. Inset: scaled spreading curves using initial filament size, R_0, and viscous timescale, τ_μ.

Data sets (A) and (C) have the same Q, but different V_N values, while data sets (B) and (C) have the same V_N, but different Q values. Increasing V_N from (A) to (C) clearly shows a decrease in the basal radius. This decrease occurs because of the reduced volume of liquid for the smaller ratio of Q/V_N, i.e., smaller R_0. Conversely, decreasing Q from (B) to (C) shows a decrease in basal radius, due to the less R_0 for lower Q. These results are in agreement with refs 6, 7, 30. In Yancheshme et al.,[5] the effect of different R_0 could be scaled out by dividing the basal radius by R_0, i.e., $R(t)/R_0$ named as spreading factor, if the Bo is constant. The inset in Figure 4 shows the spreading factor as a function of scaled time. However, we clearly see that there is no collapse of the data for the three cases discussed above, which can only be explained by a change in Bo number, as discussed in ref 5. Given that the Bo number explicitly depends on R_0 (Bo = $\rho g R_0^2/\sigma$), we must consider the effect of different printing parameters on the Bo number, i.e., the effect of gravity compared to surface tension. The corresponding Bo numbers for (A), (B), and (C) are 0.89, 0.45, and 0.26, respectively. Thus, an increase in R_0, i.e., Bo number, increases the relative effect of gravity as a driving force for spreading, and ultimately increases the basal radius.

Figure 5 shows the spreading of three different operating conditions having different values of Q and V_N, but approximately the same ratio of Q/V_N, i.e., same value of R_0 using eq 7. As it can be seen, all cases have very similar spreading dynamics. This result confirms that the spreading dynamics of filaments depends strongly, if not only, on the magnitude of Bo, which is the same result previously shown for spherical droplets.[5] Thus, the initial radius of the deposited filament, as determined by Q/V_N, ultimately determines the shape of the basal radius as a function of time. In other words, it is not any one individual parameter that determines the basal

https://doi.org/10.1021/acs.langmuir.3c00973
Langmuir 2023, 39, 10495−10503

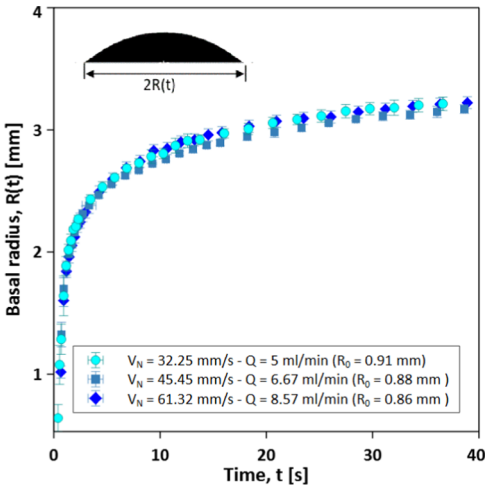

Figure 5. Basal radius as a function of time for three different extrusion cases with the same initial radius, R_0.

radius, but rather the ratio of printing parameters that define $R(t)$. This result should be strongly considered when designing experiments for optimizing printing parameters.

Dynamic Spreading of Newtonian Filaments. In the previous section, we concluded that the effect of all DIW parameters can be summarized by the Bo, which dictates the dynamics and final shape of the filament. In other words, all operating parameters simply affect R_0, which strongly affects Bond number, Bo $\propto R_0^2$. In this section, we develop a generalized theory via spreading master curves as a function of Bo, which can be used to predict the dynamic shape of deposited Newtonian filaments as a function of time. Note that we mostly limit our discussion to dynamic spreading simulations that are directly applicable to the DIW process. However, the fundamentals are applicable to the general theory of nonspherical droplet spreading.

Spreading Master Curve. There are two forces that control the shape of a filament on a substrate: gravitational ($F_g \sim \rho g R_0^3$) and capillary ($F_c \sim \sigma R_0$) forces, while two additional forces determine the spreading rate, or timescale: viscous dissipation ($F_\mu \sim \mu R_0 dR/dt$) and inertia ($F_i \sim \rho R_0^2 (dR/dt)^2$).[13] The ratio of these key forces leads to three dimensionless groups: the Bo (ratio of F_g to F_c), the Ohnsorge number, Oh, (ratio of F_μ to the square root of F_i and F_c), and the Ca (ratio of F_μ to F_c). As discussed above, Bo determines the shape of the filament, and for most practical cases, the effect of Bo cannot be ignored. Oh represents the tendency of a droplet to keep its shape. A higher Oh makes it more difficult to deform the shape, i.e., a longer time is needed to observe significant spreading. Ca is important in quantifying the deformation of the filament shape near the triple contact line. In fact, the dynamic contact angle is explicitly a function of Ca, which allows for the generalization of spreading dynamics, see eq 6.[5]

Our numerical simulations and experimental conditions will consider spreading dynamics in a regime where $0 < Bo < 1$ and $Oh > 1$, which is typical of most fluids in DIW. Note that $Oh < 1$ complicates the filament deposition process leading to very poor control of the filament shape. As discussed in ref 5, the rate of spreading can be quantified via the viscous timescale $\tau_\mu = \frac{\mu R_0}{\sigma}$. τ_μ is expected to collapse different spreading curves onto a master curve for constant Bo and constant static advancing contact angle θ_s. Therefore, time in the numerical simulations will be scaled by τ_μ, and the basal radius will be scaled by R_0.

Figure 6 shows a series of scaled basal radius master curves for different Bo and θ_s. As expected for $\theta_s = 0$, the spreading factor grows to infinity with a constant power law at long times that depends on Bo. A nonzero θ_s induces a plateau in the spreading factor, whose plateau value decreases with increasing θ_s and decreasing Bo. Increasing the Bo at constant θ_s increases both the rate of spreading and the magnitude of the spreading factor plateau. This effect is more significant at small θ_s. For example, at $\theta_s = 10°$, increasing the Bo from 0.05 to 0.9 increases the equilibrium spreading factor from 5.4 to 9.4, an 75% increase. However, at a high θ_s, i.e., 60°, the same increase in Bo results in a 20% change in the equilibrium spreading factor. The reduced effect of Bo for larger θ_s can be explained by the fact that a larger θ_s results in a larger vertical force

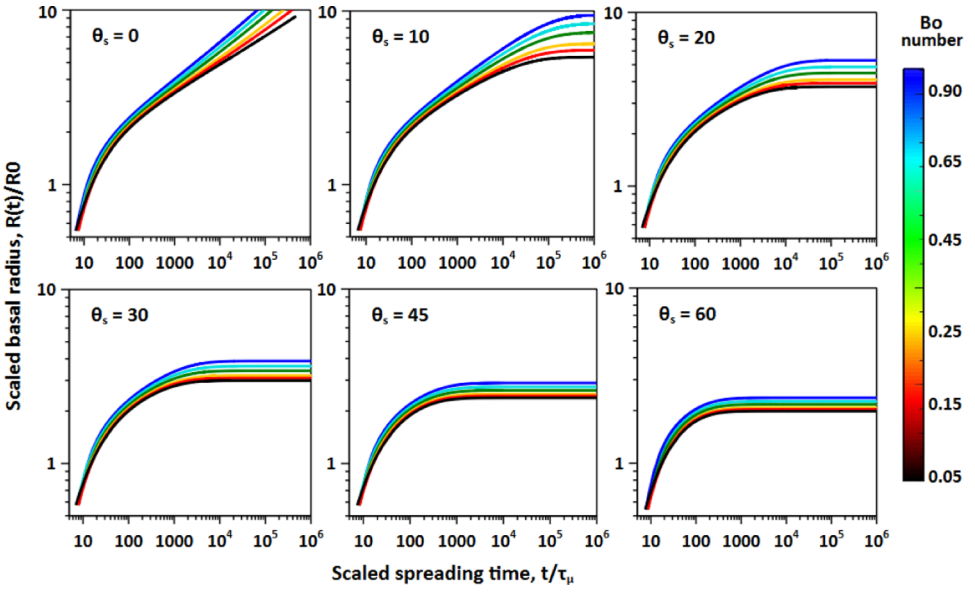

Figure 6. Effect of Bo and θ_S on the scaled master curves for filament spreading.

https://doi.org/10.1021/acs.langmuir.3c00973
Langmuir 2023, 39, 10495−10503

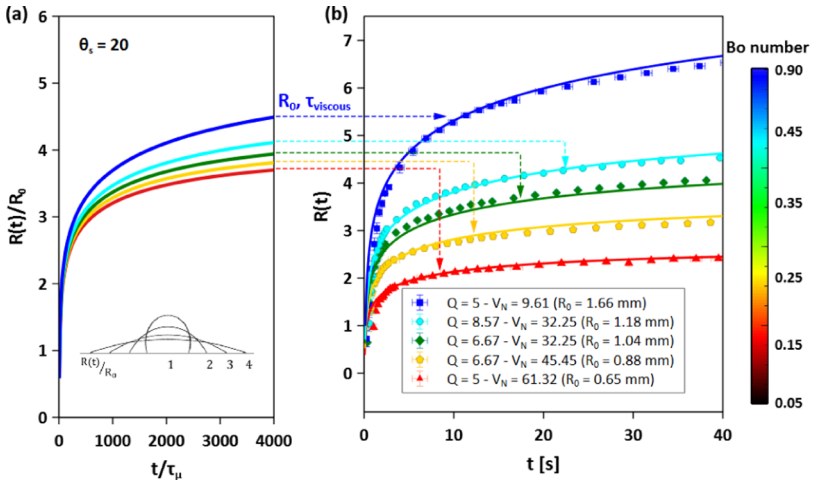

Figure 7. (a) Filament spreading master curves at different Bo and θ_s = 20°. (b) Comparison of basal radius as a function of time for different deposition parameters measured experimentally (points) and predicted using master curves (solid lines) via R_0 and τ_μ.

component from interfacial tension, i.e., σ sin θ_s, which is opposing the gravitational force downward. In other words, the effect of gravity is reduced at a larger θ_s. Thus, the result for a small θ_s is explained by the increased effect of gravity (smaller opposing vertical force from surface tension) forcing the height of the filament down and thus the basal radius out.

Figure 6 can be readily used to predict the dynamic shape of filaments. For example, the shape of a filament during DIW can be predicted by first determining the initial size of the filament, R_0 (using printing parameters, eq 7). Then, we calculate the Bo and τ_μ using the properties of the fluid and fluid−substrate, i.e., ρ, μ, σ, and θ_s. The magnitude of Bo number and θ_s determines the appropriate master curve, which can be used to predict dynamic shape or equilibrium spreading factor in dimensionless or dimensional quantities. These master curves will certainly improve the dimensional accuracy of printed parts simply by accounting for the spreading of the initial layer on the printing bed platform. This would be particularly useful for single-layer printing such as electronic boards, functional fabrics, etc.

Model Validation. Figure 7a,b compares predictions from Figure 6 with experimental data using DA-2 resin at five different operating conditions. The dimensionless curves in Figure 7a are unscaled by multiplying t by τ_s and $R(t)$ by R_0. The operating conditions, i.e., V_N and Q, were used via eq 7 to determine R_0. The Bo numbers for the data in Figure 7b are 0.15, 0.25, 0.35, 0.45, and 0.89, from red triangles to blue squares. The static advancing contact angle for this resin on silica was measured independently to be θ_s = 20°. Figure 7b compares the unscaled spreading predictions (lines) with the experimentally measured spreading curves. Note that each data set is an average of at least three experiments, and the error bars represent the standard deviation. Overall, Figure 7 shows excellent agreement between experimental results and the numerical simulations (master curves), with a maximum relative error of less than 8% for all data sets.

Final Shape Prediction. In many cases, we are simply interested in the equilibrium spreading factor and overall shape of the filament at long times, which is determined by the steady-state Young−Laplace equation.[14] The long time results from Figure 6 as well as shape information from the numerical simulations can be used to develop correlations between the equilibrium/steady-state shape of the printed filament and printing parameters. From the previous section, the equilibrium spreading factor, determined from the asymptotic value of R_f/R_0 at long times, is only a function of Bo and θ_s, which is summarized in Figure 8. As discussed above, increasing Bo and

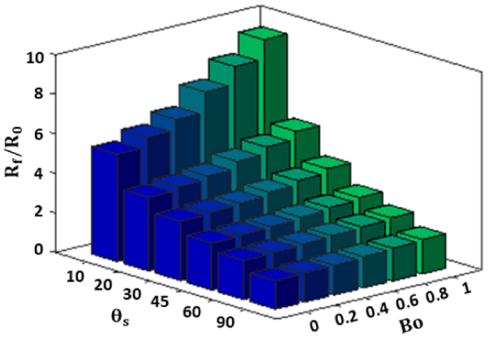

Figure 8. Steady-state (equilibrium) spreading factor (R_f/R_0) versus Bo number and θ_s.

decreasing θ_s increase the equilibrium spreading factor. Moreover, θ_s has a more significant effect on the value of R_f/R_0 than Bo. Furthermore, a decrease in θ_s weakens the effect of Bo on R_f/R_0.

Figure 9 shows the effect of θ_s on the equilibrium spreading factor for two limiting Bo numbers, i.e., Bo = 0.05 and 0.89. An analytical expression can be derived considering the case of Bo = 0, a.k.a zero-Bo assumption model. At Bo = 0, the cross section of the filament is a circular segment. Using geometrical arguments, we derived a theoretical model, eq 8, relating the equilibrium shape factor to θ_s, see Supporting Information Figure S3 for details, given by

$$\frac{R_f}{R_0} = \left(\frac{\pi}{\frac{\theta}{\sin^2\theta} - \frac{1}{\tan\theta}} \right)^{\beta} \tag{8}$$

where β = 0.5. We clearly see from Figure 9 that the numerical data for Bo = 0.05 is very well described by eq 8 and β = 0.5. However, to account for higher Bo numbers, we propose that β is a linear function of Bo. The best-fit β was determined using the generalized reduced gradient (GRG) nonlinear fitting algorithm[37] for all Bo studied in Figure 8. Figure S4, see the

https://doi.org/10.1021/acs.langmuir.3c00973
Langmuir 2023, 39, 10495−10503

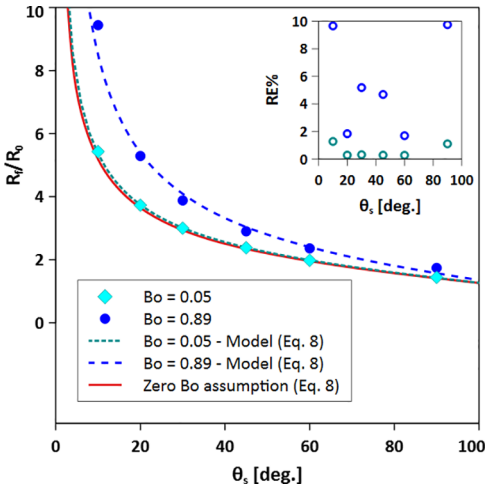

Figure 9. Simulation results of R_f/R_0 versus θ_s at two limiting Bo numbers of 0.05 and 0.89 (solid points) compared to the predictions of eq 8 and β(Bo) = 0. 17 Bo + 0.5.

Supporting Information, shows β as a linear function of Bo such that β(Bo) = 0. 17 Bo + 0.5 with the overall coefficient of determination, R^2 = 0.99. Figure 9 shows the comparison of numerical simulation data against the best-fit β parameters and eq 8 for two limiting cases, i.e., Bo = 0.05 and 0.89. The model and simulated data are in excellent agreement with the overall relative error less than 11% for a range of Bo from near zero to unity.

Comparison of the Spreading of Filaments and Droplets. We previously developed spreading master curves for Newtonian droplets and showed that the spreading is governed by Bo and θ_s.[5] It is of interest to compare the dynamics of droplet and filament spreading to better understand the effect of geometry on spreading parameters. In Figure 10, we compare the spreading of filaments and droplets having the same Bo (Bo = 0.05 and 0.5) and θ_s = 0°. It is well documented that the spreading of droplets is composed of two regimes: a fast early-stage inertia regime followed by a slow late-stage viscous regime.[5,13] Figure 10 shows two clear power-law spreading regimes for both droplets and filaments, which correspond to inertia and viscous spreading. In the inertia regime, we see very similar spreading dynamics between droplets and filaments regardless of Bo and θ_s, with a dynamic basal radius power-law scaling of nearly 0.5. In the viscous spreading regime with Bo ≪ 1, the droplet spreading dynamics follow Tanner's law, i.e., $R(t) \propto t^{0.1}$.[28] A relatively large increase in Bo for spherical droplet spreading shows only a slight deviation from Tanner's law, which is discussed in more detail elsewhere.[5] However, we see a very different result for the viscous spreading of a cylindrical filament. At the same Bo number, a cylindrical filament spreads significantly more than a spherical droplet, i.e., filament spreading has a considerably higher power-law scaling than Tanner's law, $R(t) \propto t^{0.17}$ for Bo ≪ 1. Furthermore, Bo for filament spreading has more of an effect on the spreading power-law compared to spherical droplets. The filament with Bo = 0.5 has a more than 75% increase in power-law scaling, $R(t) \propto t^{0.3}$, compared to the very small percentage (<10%) change observed in spherical droplets.

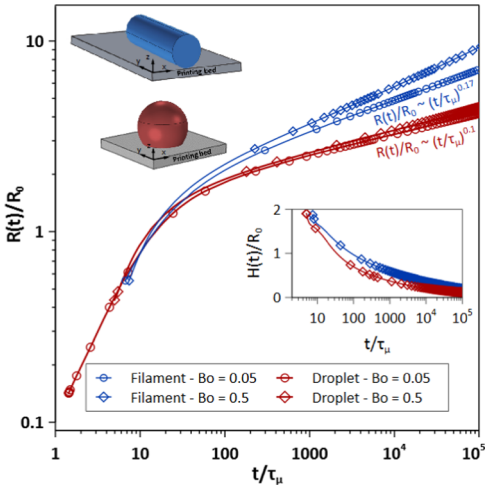

Figure 10. Spreading factor as a function to time for filament (blue) and droplet (red) at θ_s = 0° and two different Bo numbers. Inset: dimensionless height versus time at Bo = 0.5.

The larger spreading power law of filaments and its sensitivity to Bo are attributed to the differences in the geometry of the two respective coordinate systems. For example, a filament is only capable of spreading in a single Cartesian coordinate, e.g., x, while a sphere is capable of spreading in both the x and y coordinates, see schematics in Figure 10. This fact has a considerable effect on the spreading radius when we consider that the droplet and filament have similar decreases in height as a function of time. The inset of Figure 10 shows similar changes in height as a function of time for a droplet and filament with Bo = 0.5. Thus, the radius of a filament must spread more than the spherical drop to maintain conservation of volume. The effect of Bo on the power-law scaling can be understood by the same geometrical arguments since a higher Bo causes a faster decrease in height which in turn causes a faster increase in radius. In conclusion, errors in prediction are much more sensitive to the value of Bo when considering filament spreading due to the geometrical restrictions of the spreading basal radius.

CONCLUSIONS

In this work, we developed a generalized dynamic spreading model for Newtonian filaments on a flat substrate using CFD modeling and experimental validation. In fact, this work presents the first generalized model for filament spreading for both complete and partial wetting conditions, and considering the influence of gravity. The results clearly show that the scaled dynamics of filament spreading are determined by two parameters: Bo and θ_s. Increasing Bo generally leads to larger spreading factors, while increasing θ_s leads to lower spreading factors. In all cases, the spreading of a cylindrical filament is significantly larger than that observed for a spherical droplet of the same initial diameter.

These results can be used to construct dimensional spreading curves that predict the dynamic and final filament shape of real filaments. The timescale depends on the fluid properties, μ and σ, and the initial radius of the filament, R_0. R_0 is influenced by the deposition process and extrusion parameters, namely, V_N, Q, and H. When H is greater than a critical value ($2R_0$), there is no effect of H on R_0, and R_0 scales with the ratio of Q and V_N. Thus, these models can be used to predict the effect of printing parameters on final bead width and layer height in DIW or any other extrusion-based additive manufacturing method. This should significantly reduce the

https://doi.org/10.1021/acs.langmuir.3c00973
Langmuir 2023, 39, 10495−10503

trial-and-error approach and limit the printing window to a tractable, relevant space. The extension of these concepts to the spreading of non-Newtonian and reacting filaments is the subject of our ongoing research.

■ ASSOCIATED CONTENT

Supporting Information

The Supporting Information is available free of charge at https://pubs.acs.org/doi/10.1021/acs.langmuir.3c00973.

Grid independence study using evolution of basal radius (Figure S1); experimentally measured spreading dynamics of deposited filaments in terms of basal radius vs time at two different operating conditions each having three levels of nozzle heights (Figure S2); zero-Bo model for the equilibrium spreading factor of filaments (Figure S3); and values of fitting parameter β vs Bo and fitted linear model (Figure S4) (PDF)

■ AUTHOR INFORMATION

Corresponding Author

Nicolas J. Alvarez − *Chemical and Biological Engineering, Drexel University, Philadelphia, Pennsylvania 19104, United States;* orcid.org/0000-0002-0976-6542; Email: nja49@drexel.edu

Authors

Amir Azimi Yancheshme − *Chemical and Biological Engineering, Drexel University, Philadelphia, Pennsylvania 19104, United States*

Giuseppe R. Palmese − *Chemical and Biological Engineering, Drexel University, Philadelphia, Pennsylvania 19104, United States*

Complete contact information is available at: https://pubs.acs.org/10.1021/acs.langmuir.3c00973

Author Contributions

A.A.Y.: Conceptualization, methodology, software, validation, visualization, writing—original draft preparation. G.R.P.: Conceptualization, funding acquisition, writing—review & editing. N.J.A.: Conceptualization, funding acquisition, methodology, supervision, writing—review & editing.

Notes

The authors declare no competing financial interest.

■ ACKNOWLEDGMENTS

This research was sponsored by the Army Research Laboratory and was accomplished under Cooperative Agreement Number W911NF-17-2- 0227. The views and conclusions contained in this document are those of the authors and should not be interpreted as representing the official policies, either expressed or implied, of the Army Research Laboratory or the U.S. Government. The U.S. Government is authorized to reproduce and distribute reprints for Government purposes notwithstanding any copyright notation herein. N.J.A. was also supported by the National Science Foundation under grant no. CBET-1847140.

■ REFERENCES

(1) Sivasankar, V. S.; Sachar, H. S.; Sinha, S.; Hines, D. R.; Das, S. 3D printed microdroplet curing: Unravelling the physics of on-spot photopolymerization. *ACS Appl. Polym. Mater.* **2020**, *2*, 966−976.

(2) Shyam, S.; Dhapola, B.; Mondal, P. K. Magnetofluidic-based controlled droplet breakup: Effect of non-uniform force field. *J. Fluid Mech.* **2022**, *944*, A51.

(3) De Ruiter, R.; Royon, L.; Snoeijer, J. H.; Brunet, P. Drop spreading and gelation of thermoresponsive polymers. *Soft Matter* **2018**, *14*, 3096−3104.

(4) Sprittles, J. E. Dynamic wetting/dewetting processes in complex liquid-solid systems, Ph.D. thesis, University of Birmingham, 2010.

(5) Azimi Yancheshme, A.; Palmese, G. R.; Alvarez, N. J. A Generalized Scaling Theory for Spontaneous Spreading of Newtonian Fluids on Solid Substrates. *J. Colloid Interface Sci.* **2023**, *636*, 677−688.

(6) Jin, Y.; Zhao, D.; Huang, Y. Study of extrudability and standoff distance effect during nanoclay-enabled direct printing. *Bio-Des. Manuf.* **2018**, *1*, 123−134.

(7) Jang, S.; Boddorff, A.; Jang, D. J.; Lloyd, J.; Wagner, K.; Thadhani, N.; Brettmann, B. Effect of material extrusion process parameters on filament geometry and inter-filament voids in as-fabricated high solids loaded polymer composites. *Addit. Manuf.* **2021**, *47*, No. 102313.

(8) Alvarez, N. J.; Walker, L. M.; Anna, S. L. A non-gradient based algorithm for the determination of surface tension from a pendant drop: Application to low Bond number drop shapes. *J. Colloid Interface Sci.* **2009**, *333*, 557−562.

(9) Xie, J.; Randolph, R.; Simmons, G.; Vinciguerra, M.; Suri, S.; Bonini, N.; Root, A.; Hull, P. V.; Mazzeo, A. D. Spreading of fast-curing, thermosetting silicones. *Appl. Phys. Lett.* **2019**, *115*, No. 253701.

(10) Lewis, J. A. Direct ink writing of 3D functional materials. *Adv. Funct. Mater.* **2006**, *16*, 2193−2204.

(11) Li, L.; Lin, Q.; Tang, M.; Duncan, A. J.; Ke, C. Advanced polymer designs for direct-ink-write 3D printing. *Chem. - Eur. J.* **2019**, *25*, 10768−10781.

(12) Layani, M.; Wang, X.; Magdassi, S. Novel materials for 3D printing by photopolymerization. *Adv. Mater.* **2018**, *30*, No. 1706344.

(13) Biance, A.-L.; Clanet, C.; Quéré, D. First steps in the spreading of a liquid droplet. *Phys. Rev. E* **2004**, *69*, No. 016301.

(14) Young, T., III. An essay on the cohesion of fluids. *Philos. Trans. R. Soc. London* **1805**, 65−87.

(15) Starov, V.; Tyatyushkin, A.; Velarde, M.; Zhdanov, S. Spreading of non-Newtonian liquids over solid substrates. *J. Colloid Interface Sci.* **2003**, *257*, 284−290.

(16) Gennes, P.-G.; Brochard-Wyart, F.; Quéré, D. et al. *Capillarity and Wetting Phenomena: Drops, Bubbles, Pearls, Waves*; Springer, 2004.

(17) Eddi, A.; Winkels, K. G.; Snoeijer, J. H. Short time dynamics of viscous drop spreading. *Phys. Fluids* **2013**, *25*, No. 013102.

(18) Shi, L.; Liu, Y.; Lu, H.; Meng, Y.; Hu, G.; Tian, Y. Viscous force retards initial droplet spreading. *J. Phys. Chem. C* **2017**, *121*, 22054−22059.

(19) Erickson, D.; Blackmore, B.; Li, D. An energy balance approach to modeling the hydrodynamically driven spreading of a liquid drop. *Colloids Surf., A* **2001**, *182*, 109−122.

(20) Madejski, J. Solidification in flow through channels and into cavities. *Int. J. Heat Mass Transfer* **1976**, *19*, 1351−1356.

(21) Gu, Y.; Li, D. A model for a liquid drop spreading on a solid surface. *Colloids Surf., A* **1998**, *142*, 243−256.

(22) Gu, Y.; Li, D. Liquid drop spreading on solid surfaces at low impact speeds. *Colloids Surf., A* **2000**, *163*, 239−245.

(23) Voinov, O. V. Gravity-induced spreading of a drop of a viscous fluid over a surface. *J. Appl. Mech. Tech. Phys.* **1999**, *40*, 412−419.

(24) Voinov, O. V. Hydrodynamics of wetting. *Fluid Dyn.* **1977**, *11*, 714−721.

(25) Cox, R. G. The dynamics of the spreading of liquids on a solid surface. Part 1. Viscous flow. *J. Fluid Mech.* **1986**, *168*, 169−194.

(26) Shyam, S.; Gaikwad, H. S.; Ghalib Ahmed, S. A.; Chakraborty, B.; Mondal, P. K. Investigations into the complete spreading dynamics of a viscoelastic drop on a spherical substrate. *Langmuir* **2021**, *37*, 63−75.

(27) Winkels, K. G.; Weijs, J. H.; Eddi, A.; Snoeijer, J. H. Initial spreading of low-viscosity drops on partially wetting surfaces. *Phys. Rev. E* **2012**, *85*, No. 055301.
(28) Tanner, L. H. The spreading of silicone oil drops on horizontal surfaces. *J. Phys. D: Appl. Phys.* **1979**, *12*, 1473.
(29) Wang, J.; Shaw, L. L. Rheological and extrusion behavior of dental porcelain slurries for rapid prototyping applications. *Mater. Sci. Eng., A* **2005**, *397*, 314−321.
(30) Khalil, S.; Sun, W. Biopolymer deposition for freeform fabrication of hydrogel tissue constructs. *Mater. Sci. Eng., C* **2007**, *27*, 469−478.
(31) Bonada, J.; Xuriguera, E.; Calvo, L.; Poudelet, L.; Cardona, R.; Padilla, J. A.; Niubó, M.; Fenollosa, F. Analysis of printing parameters for metal additive manufactured parts through Direct Ink Writing process. *Procedia Manuf.* **2019**, *41*, 666−673.
(32) Jiang, Y.; Hu, S.; Pan, Y. A normalized trace geometry modeling method with bulge-free analysis for direct ink writing process planning. *3D Print. Addit. Manuf.* **2018**, *5*, 301−310.
(33) Tu, J.; Makarian, K.; Alvarez, N. J.; Palmese, G. R. Formulation of a model resin system for benchmarking processing-property relationships in high-performance photo 3D printing applications. *Materials* **2020**, *13*, 4109.
(34) Derby, B. Inkjet printing of functional and structural materials: fluid property requirements, feature stability, and resolution. *Annu. Rev. Mater. Res.* **2010**, *40*, 395−414.
(35) Comminal, R.; Serdeczny, M. P.; Pedersen, D. B.; Spangenberg, J. Numerical modeling of the strand deposition flow in extrusion-based additive manufacturing. *Addit. Manuf.* **2018**, *20*, 68−76.
(36) Serdeczny, M. P.; Comminal, R.; Pedersen, D. B.; Spangenberg, J. Experimental validation of a numerical model for the strand shape in material extrusion additive manufacturing. *Addit. Manuf.* **2018**, *24*, 145−153.
(37) Lasdon, L. S.; Fox, R. L.; Ratner, M. W. Nonlinear optimization using the generalized reduced gradient method. *R.A.I.R.O. Recherche opérationnelle* **1974**, *8*, 73−103.

https://doi.org/10.1021/acs.langmuir.3c00973
Langmuir 2023, 39, 10495−10503